

# Array-conditioned deconvolution of multiple-component teleseismic recordings

C.-W. Chen,<sup>1\*</sup> D. E. Miller,<sup>2</sup> H. A. Djikpesse,<sup>2</sup> J. B. U. Haldorsen<sup>2</sup> and S. Rondenay<sup>1</sup>

<sup>1</sup>Department of Earth, Atmospheric and Planetary Sciences, Massachusetts Institute of Technology, Cambridge, MA 02139, USA.

E-mail: cwchen@dtm.ciw.edu

<sup>2</sup>Department of Mathematics and Modeling, Schlumberger-Doll Research, Cambridge, MA 02139, USA

Accepted 2010 May 3. Received 2010 March 5; in original form 2009 October 18

## SUMMARY

We investigate the applicability of an array-conditioned deconvolution technique, developed for analysing borehole seismic exploration data, to teleseismic receiver functions and data pre-processing steps for scattered wavefield imaging. This multichannel deconvolution technique constructs an approximate inverse filter to the estimated source signature by solving an overdetermined set of deconvolution equations, using an array of receivers detecting a common source. We find that this technique improves the efficiency and automation of receiver function calculation and data pre-processing workflow. We apply this technique to synthetic experiments and to teleseismic data recorded in a dense array in northern Canada. Our results show that this optimal deconvolution automatically determines and subsequently attenuates the noise from data, enhancing  $P$ -to- $S$  converted phases in seismograms with various noise levels. In this context, the array-conditioned deconvolution presents a new, effective and automatic means for processing large amounts of array data, as it does not require any ad-hoc regularization; the regularization is achieved naturally by using the noise present in the array itself.

**Key words:** Time series analysis; Body waves; Coda waves; Cratons; Crustal structure; North America.

## 1 INTRODUCTION

A number of methodologies have been developed over the years to analyse converted seismic waves, ranging from single station applications to high-resolution imaging using dense arrays of broad-band seismometers. Such developments have been made possible by the increased availability of teleseismic data recorded at dense broadband seismic arrays. We refer the reader to Rondenay (2009) for a comprehensive review of processing steps that have been developed to obtain images of discontinuities in the Earth's subsurface from data consisting of seismograms sampled by dense arrays of recorders. Of particular interest are methods focused on  $P$ -to- $S$  ( $P_S$ ) conversion in the coda of teleseismic  $P$  waves, due to its generally high signal-to-noise ratio and lack of contamination from later arriving primary phases. Such signal was first used for direct imaging in landmark studies by Vinnik (1977) and Langston (1979). To increase the signal-to-noise ratio of converted phases, these authors combined records from multiple sources by stacking traces that were source-normalized and time-shifted according to incidence angle. The term receiver function (RF) was introduced by Langston (1979)

to describe these normalized records of converted waves and their stacks.

A key step in the RF processing chain is the ‘source-normalization’, which requires the construction and application of a deconvolution operator to remove the extended earthquake source function, replacing it with an approximate impulse. The increasing amount of dense array data has motivated the development of new multichannel deconvolution methods, such as simultaneous deconvolution (Bostock & Sacchi 1997), autocorrelation stacking (Li & Nábělek 1999) and pseudostation stacking (Neal & Pavlis 1999, 2001). Here, we examine a multichannel deconvolution method originally developed for analysing borehole seismic exploration data. Fig. 1 illustrates this deconvolution step using data from the POLARIS-MIT seismic array in the Slave province, Canada. Fig. 1(a) shows the  $P$  and  $SV$  component data from a single earthquake recorded at 18 stations, after application of the free surface transfer matrix method (Kennett 1991) to partition the three-component records into  $P$ - $SV$ - $SH$  wavefields. The effective source function clearly rings for more than a minute, mainly due to reverberation in the crust near the source. Fig. 1(b) shows the same data after application of a deconvolution operator derived by the method of Haldorsen *et al.* (1994, 1995), as discussed herein. The deconvolved  $SV$  data show a clear arrival at  $\sim 4.8$  s, resulting from  $P$  to  $SV$  conversion at the Moho discontinuity. It is the purpose

\*Now at: Department of Terrestrial Magnetism, Carnegie Institution of Washington, Washington, DC 20015, USA.

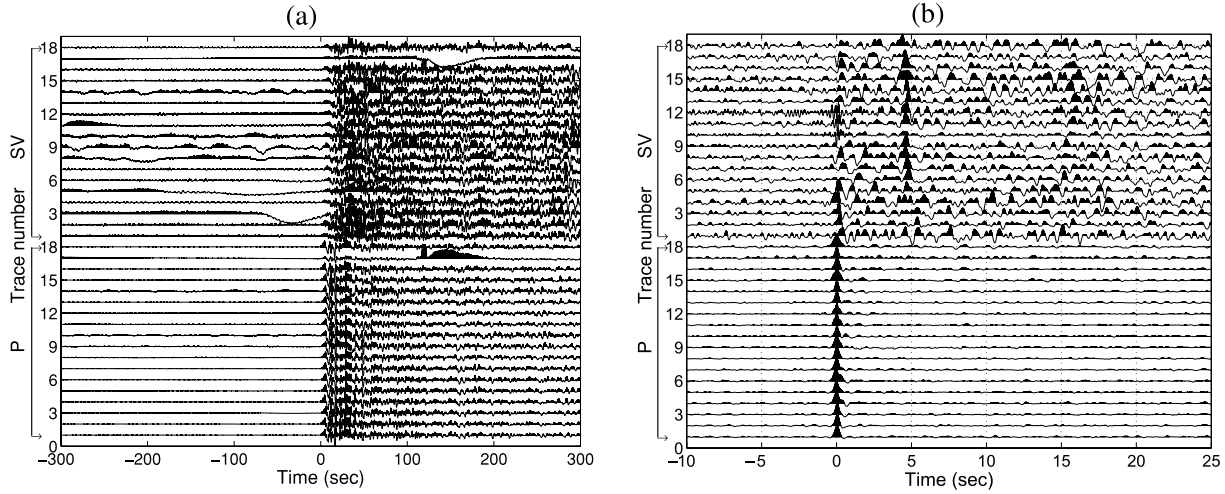


**Figure 1.** (a) The  $P$ - and  $SV$ -component data of a Japan ( $m_b = 6.5$ , 36-km deep) earthquake. (b) The deconvolved  $P$ - and  $SV$ -component data of (a).

of this paper to discuss this deconvolution method in the context of teleseismic data and to describe its application to data from the POLARIS-MIT array.

## 2 METHODOLOGIES

Our study focuses on investigating the effectiveness of the array-conditioned deconvolution, in comparison with conventional frequency-domain deconvolution method, that is, the water level deconvolution. Thus, in this section, we first provide a review of the water level deconvolution method, and then introduce the array-conditioned deconvolution.

### 2.1 Water level deconvolution

Deconvolution is usually cast as a solution to the forward expression (*cf.* Rondenay 2009, section 5):

$$d(t) = w(t) \times r(t) + n(t), \quad (1)$$

in which the observed signal  $d(t)$  is expressed as the convolution of an Earth impulse response  $r(t)$  with a source signature  $w(t)$ . In eq. (1),  $n(t)$  represents residual energy, typically assumed to be Gaussian random noise with zero-mean. The normalization process to solve for  $r(t)$  involves deconvolving  $w(t)$  from  $d(t)$ . For the ideal case, that is, there is no noise, the source signature and the observed signal are known and not frequency band limited, this problem may be solved directly by division in the frequency domain. However, the deconvolution procedure is usually ill-posed because of the presence of random noise, frequency bandwidth limitation and inaccuracies in estimation of source signature. Therefore, the process has to be regularized. This is usually achieved in the frequency domain by pre-whitening the amplitude spectrum of the source wavelet, to avoid small amplitudes that would cause numerical instabilities and ringing in the deconvolved signal. Hereafter, we will only be using signals in the frequency domain. For simplicity, we shall keep the same notation for the variables in eq. (1).

An approximate solution of the impulse response  $\hat{r}$  is expressed as (e.g. Berkhoult 1977)

$$\hat{r}(\omega) = \frac{w^*(\omega)}{w(\omega)w^*(\omega) + \delta} d(\omega), \quad (2)$$

where the asterisk denotes the complex conjugate,  $\omega$  is angular frequency and  $\delta$  is a regularization factor. The factor, sometimes

termed water level (Clayton & Wiggins 1976), represents the expected noise power. When  $\delta$  is zero, eq. (2) is a simple spectral division solving the equation  $d(\omega) = w(\omega)r(\omega)$ . When  $\delta$  is large, the denominator in eq. (2) is approximately constant and eq. (2) becomes a convolution with the estimated source.

The method assumes that the noise spectrum is white and requires either independent knowledge of the noise power or a search for the ‘best’ parameter that stabilizes the deconvolution process. This is usually done on a trial and error basis, and thus is subjective and labour-intensive. It is desirable to introduce more objective means to estimate the regularization parameter. For example, Bostock (1998) considered a family of recorded traces  $d_m(\omega)$  and associated source estimates  $w_m(\omega)$  and proposed choosing  $\delta$  by minimizing the generalized cross-validation function GCV ( $\delta$ ) shown as

$$GCV(\delta) = \frac{\sum_{m=1}^M \sum_{l=1}^L [d_m(\omega_l) - w_m(\omega_l)\hat{r}(\omega_l)]^2}{[ML - \sum_{l=1}^L X(\omega_l)]^2}, \quad (3)$$

where

$$X(\omega) = \frac{\sum_{m=1}^M w_m(\omega)w_m^*(\omega)}{\sum_{m=1}^M w_m(\omega)w_m^*(\omega) + \delta}, \quad (4)$$

with  $M$  denoting the number of traces and  $L$  is the number of frequencies represented in the discrete Fourier transform. This process does not require any assumption concerning the noise level in the data, but it still assumes a white noise spectrum and requires an iterative grid search to obtain the value for  $\delta$  (within a given range) that results in the minimal GCV.

### 2.2 Array-conditioned deconvolution

Haldorsen *et al.* (1994, 1995) described a method for exploiting the redundancy in seismic array data to obtain an optimized deconvolution filter by using the data to estimate both the source and noise spectra without assuming that either is white. That method may be summarized as follows.

Suppose we are given data recorded at an array of receivers and time-shifted and normalized such that each observed trace  $d_m(t)$  can be assumed to contain a common source signature  $w(t)$ , superposed with a variable ‘noise’  $n_m$ . That is, we are given a subscripted array of equations, like eq. (1):

$$d_m(t) = w(t) + n_m(t). \quad (5)$$

Here  $r(t)$  from eq. (1) is assumed to be an impulse. Thus, all aligned signals contributing to the source estimation are assumed to be part of the source signature. Additional copies shifted and misaligned (e.g. multipath signal arriving obliquely across the array) are formally part of the ‘noise’, but will be preserved and spiked in so far as they carry the same signature as the aligned signal. Similarly, the filter derived from the aligned  $P$  data can be applied to  $SV$  data to compress and enhance the converted signal carrying the same source signature, yielding a compressed arrival with the delay relative to the aligned signal preserved by the deconvolution operator.

In the frequency domain, this data model is written as a set of equations,

$$d_m(\omega) = \hat{w}(\omega) + n_m(\omega). \quad (6)$$

Here we have replaced  $w$  with  $\hat{w}$  to emphasize the need for an estimate of the signal and the mathematical relationship between the signal estimate  $\hat{w}$  and the filter estimate  $W(\omega)$  defined as follows. Given an estimate  $\hat{w}$  for  $w$ , a deconvolution filter  $W$  can be determined, independently for each  $\omega$ , as the solution to the set of eq. (6) constrained by the equations

$$W(\omega)d_m(\omega) = 1. \quad (7)$$

These equations have the least-squares solution (e.g. Press *et al.* 1992)

$$W(\omega) = \frac{\hat{w}^*(\omega)}{E_T(\omega)}, \quad (8)$$

where the caret denotes estimate, and  $E_T(\omega)$  is the average total energy of the raw traces,

$$E_T(\omega) = \frac{1}{M} \sum_{m=1}^M |d_m(\omega)|^2. \quad (9)$$

Substituting  $d_m$  in eq. (9) with the expression in eq. (6), eq. (8) can be rewritten as

$$W(\omega) = \frac{\hat{w}^*(\omega)}{|\hat{w}(\omega)|^2 + E_N(\omega)}, \quad (10)$$

where

$$E_N(\omega) = \frac{1}{M} \sum_{m=1}^M |d_m(\omega) - w(\omega)|^2. \quad (11)$$

This agrees with eq. (2) when  $E_N(\omega)$  is a constant, independent of  $\omega$ , and thus represents a data-adaptive solution to the filter regularization problem, which is applicable in a wider context than is the water level deconvolution.

The properties of this optimum filter are discussed in detail in Haldorsen *et al.* (1994). In particular, one can rearrange eq. (8) to give

$$W(\omega) = \frac{\hat{w}^*(\omega)}{|\hat{w}(\omega)|^2} D(\omega), \quad (12)$$

where the frequency domain semblance  $D(\omega)$  is given by

$$D(\omega) = \frac{|\hat{w}(\omega)|^2}{E_T(\omega)}. \quad (13)$$

The optimum filter in eq. (12) is thus recognized as a spectral division filter, multiplied by the semblance, which acts as a data-adaptive, band-limiting filter attenuating frequencies where the signal-to-noise ratio is small.

In the original discussion, the source estimate and the filter construction were derived together, assuming that all the data from a

single recorded component were used in constructing both the numerator and the denominator of the filter (eq. 8). As noted, however, these two aspects of the filter construction can be uncoupled and treated separately. Once we have the signature estimate  $\hat{w}$ , the filter obtained by eq. (8) is least-squares optimal for that estimate, independently of how the estimate was obtained.

Thus, the traces used to estimate  $\hat{w}$  may be distinct from those used in estimating  $E_T$ . Moreover, the filter itself may be applied to traces that are distinct from the traces used to estimate  $\hat{w}$ . In particular, when, as in the case of teleseismic data, it may be reasonably assumed that a complicated packet of energy is converted from  $P$  to  $S$  somewhere near the receiver array, the  $P$  arrivals can be aligned and used to estimate the signature while the complete ensemble of multiple-component data is used in estimating the total energy. Note, however, that stability is only guaranteed if the source estimation traces are included in the estimate for total energy.

In the next section, we carry out synthetic experiments to evaluate the performance of the array-conditioned deconvolution and to compare the results with those using water level deconvolution.

### 3 SYNTHETIC EXPERIMENTS

We construct the synthetic waveforms by using forward-modelled Earth impulse responses, as well as observed seismograms from the 2005 August 16 earthquake ( $m_b = 6.5$ ) in Japan, recorded at 18 stations of the POLARIS-MIT array in the Slave province, Canada. We perform deconvolution on this synthetic data set with the addition of various levels of noise. The procedure of the synthetic waveform construction is as follows:

(1) We compute the synthetic  $P$  and  $SV$  impulse responses using Zoeppritz reflection and transmission coefficients (e.g. Aki & Richards 2002) calculated for a simple two-layer velocity model and a single horizontal slowness representative of the field data. Fig. 2(a) shows the result of this computation. The  $P$  component has the direct  $P$  wave ( $\dot{P}$ ) and the first-order multiples that end with  $P$  ( $\dot{P}\dot{P}\dot{P}$ ,  $\dot{P}\dot{S}\dot{P}$ ,  $\dot{S}\dot{P}\dot{P}$ ,  $\dot{S}\dot{S}\dot{P}$ ). The  $S$  component has the converted  $S$  wave ( $\dot{S}$ ) and the first-order multiples that end with  $S$  ( $\dot{P}\dot{P}\dot{S}$ ,  $\dot{P}\dot{S}\dot{S}$ ,  $\dot{S}\dot{P}\dot{S}$ ,  $\dot{S}\dot{S}\dot{S}$ ). Note that the kinematically identical arrivals (e.g.  $\dot{P}\dot{S}\dot{S}$  and  $\dot{S}\dot{P}\dot{S}$ ) combine so that there are four arrivals in each mode. Note also that each  $P$  arrival has a corresponding  $S$  arrival obtained by replacing the last  $P$  segment with an  $S$  segment, hence the relative time delay is the same in all cases.

(2) We align the  $P$ -component seismograms of the Japan event and derive a ‘synthetic’ source signature through diversity stack (Embree 1968) of the aligned seismograms. The diversity stack is derived as a least-squares optimal estimate of the signal from aligned traces with constant signal and variable noise (Embree 1968). For each trace, the averaging weight is inversely proportional to the total energy in the trace. For the Slave craton data, we compared the diversity stack with mean, median and the first eigenvector estimates (Ulrych *et al.* 1999; Rondenay *et al.* 2005) and found no significant difference between these methods, except that the median estimate retains more high-frequency noise. This synthetic source signature thus represents the noise-free common source signal (Fig. 2b).

(3) We convolve the synthetic source signal with the synthetic  $P$  and  $SV$  impulse responses to yield the noise-free synthetic data (Fig. 2c).

(4) We extract 300-s long data before the  $P$  arrival from each trace of the  $P$ - and  $SV$ -component seismograms of the Japan event recorded by the POLARIS-MIT array, to be representative of

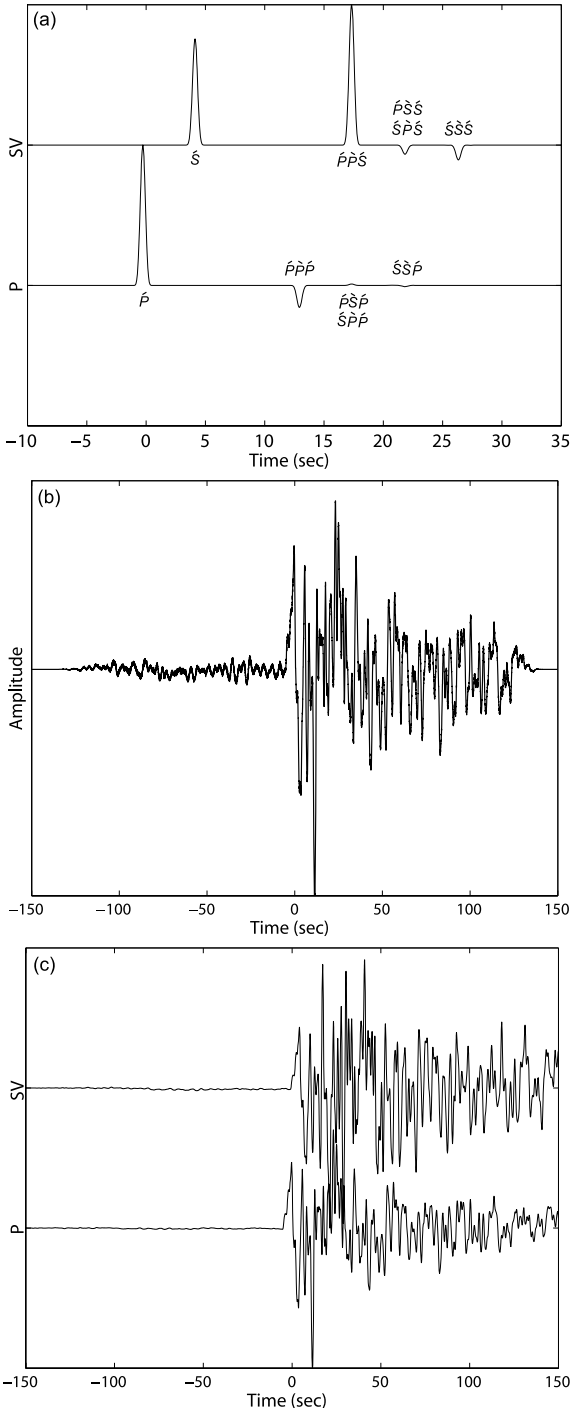


**Figure 2.** (a) The synthetic  $P$ - and  $SV$ -component impulse responses for an incident  $P$  wave of ray parameter  $p = 0.06 \text{ s km}^{-1}$ , sampling an isotropic two-layer model. The model consists of a 40-km thick horizontal layer ( $\alpha_0 = 6.6 \text{ km s}^{-1}$ ,  $\beta_0 = 3.7 \text{ km s}^{-1}$ ,  $\rho_0 = 2600 \text{ kg m}^{-3}$ ) over a half-space ( $\alpha_1 = 8.1 \text{ km s}^{-1}$ ,  $\beta_1 = 4.5 \text{ km s}^{-1}$ ,  $\rho_0 = 3500 \text{ kg m}^{-3}$ ). (b) The source signature estimate used to construct the synthetic array data. (c) The noise-free synthetic data constructed from convolving (a) with (b).

background noise. We also subtract the synthetic source signal from the respective observed  $P$ -component seismogram, and the residuals obtained are representative of additional incoherent noise between traces. We combine these two types of noise, randomly shift

them in the time domain and add a scaling factor  $\lambda$  for controlling the amplitude, before adding them to the noise-free synthetic data. As such, we generate synthetic seismograms with characteristics of an actual earthquake and actual noise variations across an array. The complete synthetic data model for the  $P$  component [ $d_p(t)$ ] and  $SV$  component [ $d_{sv}(t)$ ] can be thus described as, respectively,

$$d_p(t) = \hat{w}(t) \times g_p(t) + \lambda N_p(t); \quad (14)$$

and

$$d_{sv}(t) = \hat{w}(t) \times g_{sv}(t) + \lambda N_{sv}(t), \quad (15)$$

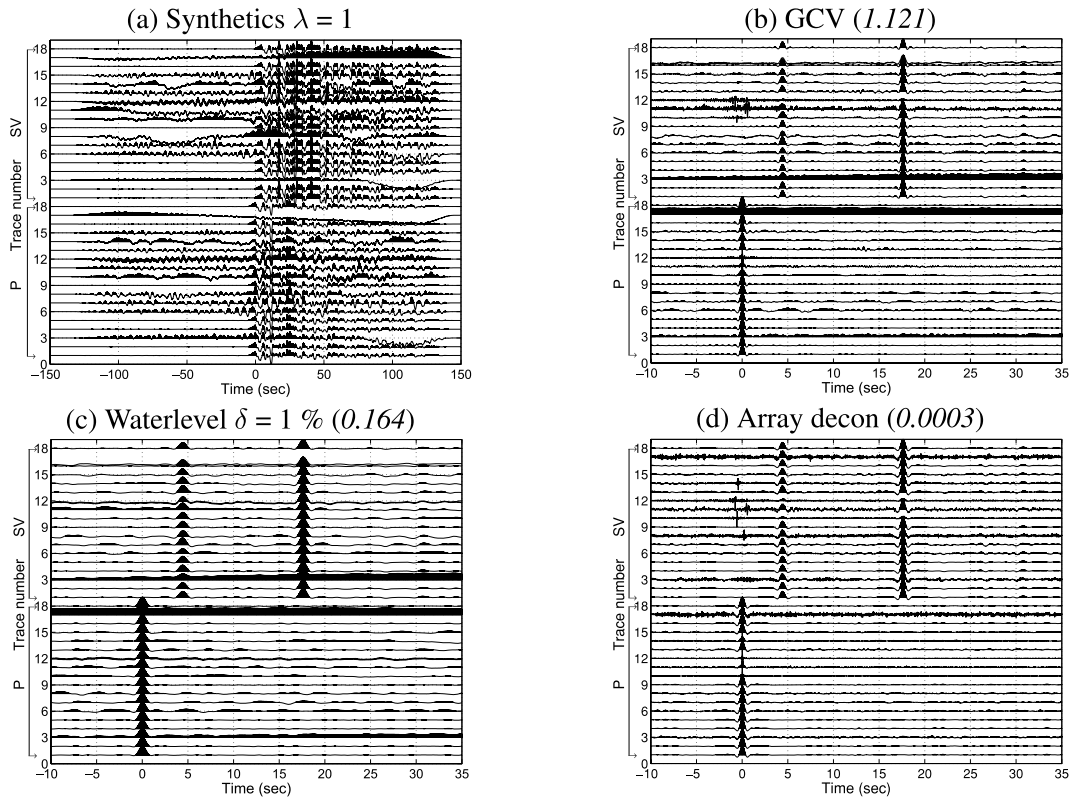
where  $g_p(t)$  and  $g_{sv}(t)$  are the synthetic  $P$  and  $SV$  impulse responses, and  $N_p(t)$  and  $N_{sv}(t)$  are the total (combined and shifted) noise in  $P$  and  $SV$  components. By changing the scaling factor  $\lambda$ , we are able to generate synthetic data with various noise levels to test the effectiveness of the deconvolution methods. Note that  $\lambda$  does not change the spectral content of the noise.

Fig. 3 summarizes the results of the synthetic experiments. Fig. 3(a) shows the synthetic array data ( $P$  and  $SV$  components) with noise level  $\lambda = 1$ . Figs 3(b) and (c) show the deconvolution results using the water level method with the GCV-derived  $\delta$  parameter and with water level of 1 per cent of the maximum amplitude of the source signature estimate, respectively. Fig. 3(d) shows the result using the array deconvolution. This synthetic test allows us to make the following observations. First, the GCV yields trace-dependent  $\delta$  values that are equivalent to 0.001–0.01 per cent of the maximum amplitude of the source estimate. Second, while the water level method in general recovers the impulse response in most  $SV$  traces, it fails to resolve traces that are anomalously noisy, for instance, traces 3 and 17. Furthermore, as the water level factor increases, the deconvolved signal broadens and loses resolution. This is expected because using a higher water level amounts to pre-whitening more high-frequency signals. In a sense, it becomes a low-pass filter, removing high-frequency content in the data. Conventionally, this process of iterating over a number of water level factors is conducted and visual inspection is required until a ‘best’ water level is determined. On the other hand, the array deconvolution (Fig. 3d) does not require any iterative process or human intervention, and stabilizes noisy traces while better resolving the impulse response consistently across the array. Here,  $E_T(\omega)$  is calculated using  $P$ -component data.

Note that, in the deconvolution process,  $\hat{w}(t) \times g_p(t)$  becomes the effective source signature, and that relative amplitudes in the deconvolved  $SV$  data are slightly altered from those of  $g_{sv}(t)$ . This is an issue for any deconvolution process. The consistency achieved by using a single deconvolution operator for all receivers should enable further analysis beyond the scope of this paper.

Similar results are observed when we increase the noise in the synthetic data. The water level deconvolution becomes unstable, that is, the deconvolved traces are more ringing, whereas the array deconvolution still achieves similar resolution.

One way to evaluate the performance of the deconvolution filters is to measure the variance between the deconvolved signals across the array. We calculate the variance by summing the square of the difference between each trace and the mean trace. The corresponding variance of each deconvolved data section is shown as the number in the parentheses above each panel in Fig. 3. The array deconvolution yields a much better, that is, smaller, variance than those from the other two approaches. For water level deconvolution, we



**Figure 3.** Summary of the synthetic experiments. (a) The synthetic array data of  $\lambda = 1$ . The deconvolved data section using (b) water level deconvolution with GCV-derived  $\delta$ ; (c) water level deconvolution with the factor of 1 per cent and (d) array-conditioned deconvolution. The number in the parentheses indicates the corresponding variance.

note that there appears to be a trade-off between variance and broadening of the deconvolved signal; larger water level results in smaller variance but less sharp impulse. The choice of the optimal water level is thus based on this trade-off: when increasing water level beyond a certain value does not reduce the variance significantly, we designate this value as the optimal water level to use (1 per cent in this synthetic case). In contrast, array-conditioned deconvolution always achieves small variance and sharper impulse. Fig. 4 shows the comparison of the amplitude spectra of deconvolved signals of trace three (Fig. 3) derived from the array approach and the water level approach, respectively, along with the amplitude spectrum of the raw synthetic trace. The spectra are normalized by the amplitude at 0.5 Hz of each trace. The raw synthetic data is dominated by low-frequency noise, and the array deconvolution, compared with the water level method, achieves a better resolution of the impulse without sacrificing much higher frequency (0.5–1.5 Hz) content. We emphasize that, since array deconvolution estimates a different noise energy for each frequency, whereas water level deconvolution uses a single noise parameter for all frequencies, the difference between array deconvolution and optimal water level deconvolution is most significant when the source time function and/or noise is not spectrally flat. In particular, this is true when the signature contains near-source reverberation.

In this section, we have demonstrated the effectiveness of the array-conditioned deconvolution, especially for noisy data. In the following section, we apply this deconvolution to a field data set of the Slave province. In this example, we focus our demonstration on the  $P$ - and  $SV$ -component seismograms, but note that the method is readily applicable to  $SH$  components as well.

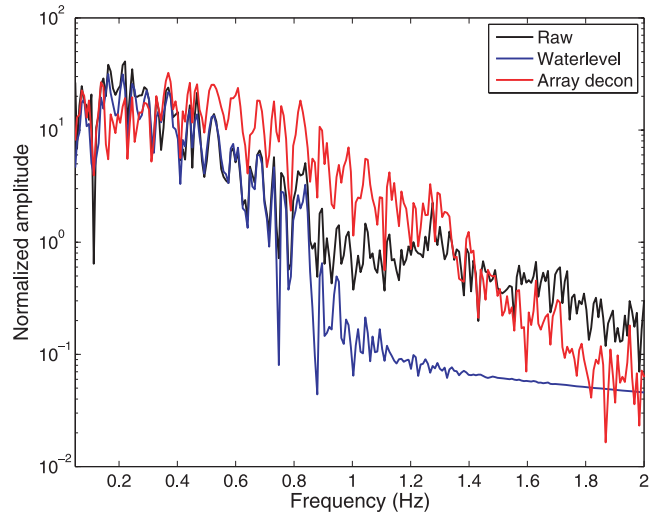


**Figure 4.** Comparison of the amplitude spectra of the deconvolved  $SV$  signals of trace three, derived from the array deconvolution and the water level deconvolution, respectively. The amplitude spectrum of the ‘raw’ synthetic trace is also plotted. The spectra are normalized by the amplitude at 0.5 Hz of each trace. Note that the spectra have been decimated by a factor of 5.

#### 4 APPLICATION TO THE SLAVE CRATON ARRAY DATA

We use seismic array data recorded in the Slave province, an Archean craton which is located in the northwestern Canadian

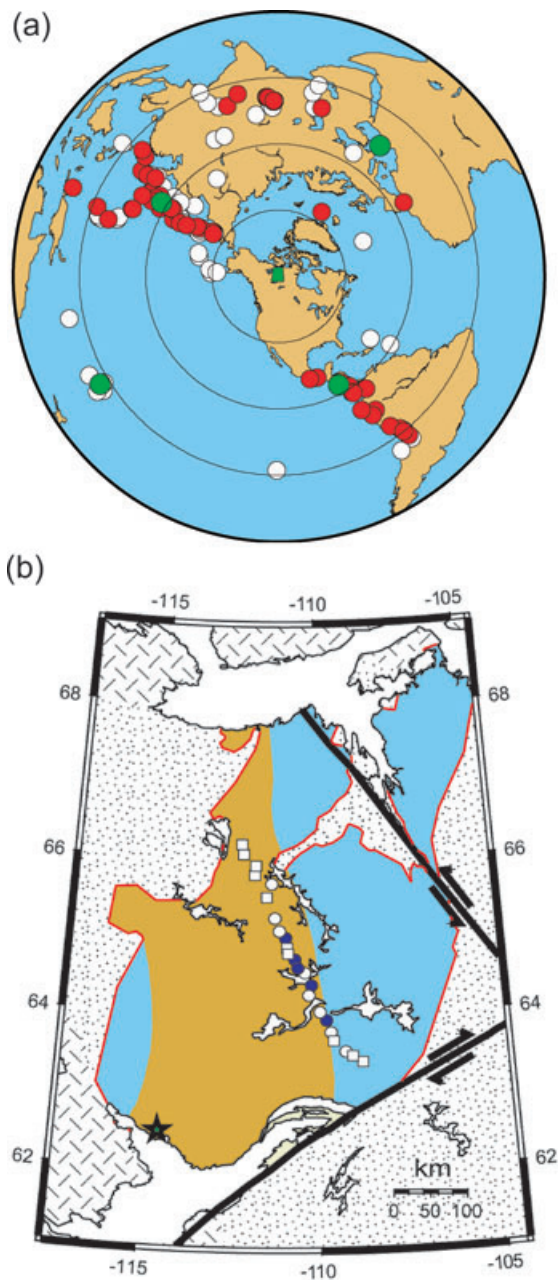


**Figure 5.** (a) The earthquake event distribution projected with the Slave craton in the centre (green square). The red circles denote events used in the previous receiver function study (Chen *et al.* 2009). The white circles denote the additional events that are analysed by the array deconvolution. The green circles denote the four exemplary events whose data are shown in Fig. 6. The combined data set includes a total of 135 events. (b) Simplified geological map of the Slave craton (outlined in red). The brown shaded area is the central Slave basement complex (CSBC; Bleeker *et al.* 1999), which is the oldest portion (2.6–4 Ga) of the craton. The blue shaded area denotes the eastern Slave craton which is covered by juvenile crust. The seismic stations used in this study are denoted in squares (MIT stations) and circles (POLARIS stations). The five stations denoted in blue are those whose data are shown in Fig. 8. From south to north, these stations are BOXN, LGSN, LDGN, EKTN and ACKN.

Shield (Fig. 5a). The Slave craton has been the subject of intensive geophysical and petrological studies due to its longevity and the presence of abundant diamondiferous kimberlites. The POLARIS-MIT seismic array (Fig. 5b) in the Slave craton con-

sists of 23 seismic stations, each equipped with a three-component broad-band seismometer. A previous receiver-function study (Chen *et al.* 2009) identified a distinct crust–mantle boundary, or Moho, at  $\sim 4.8$  s across the array, using water level deconvolution and common-conversion-depth stacks of high-quality data from 62 teleseismic events with magnitude  $m_b \geq 5.8$  recorded during 2004–2006. Now, using the new array-conditioned deconvolution method, we are able to analyse data from 135 events with magnitude  $m_b \geq 5.5$  (Fig. 5a) during the same recording period. We use the event locations provided by the USGS PDE catalogue, and rotate the horizontal-component data to radial and transverse components (vertical component remains the same). We subsequently partition the components into  $P$ ,  $SV$  and  $SH$  wavefields by the free surface transfer matrix (Kennett 1991). After wavefield partition, we align the data by the predicted arrival times calculated in a 1-D global reference model (e.g. iasp91, Kennett & Engdahl 1991). The source signature is estimated from the  $P$  component by diversity stack (Embree 1968), and the noise energy is calculated from the  $P$ -component data. The deconvolution is then performed to yield deconvolved  $P$  and  $S$  signals. We observe that the deconvolved  $P$  impulses across the array often show time differences between each other, indicating inaccurate original reference alignment. Therefore, in practice, the deconvolved  $P$  impulses are iteratively realigned by adjusting their time lags, and a subsequent deconvolution is performed to yield the final results.

Fig. 6 shows the raw data of four example earthquakes (Table 1). These raw data show different characteristics of the coherently aligned signals in the  $P$  components, marking the various earthquake source signatures, as well as different patterns and amplitudes of the background noise in the  $SV$  components. Fig. 7 shows their deconvolved results from array deconvolution, compared with those from water level deconvolution. The results of earthquake data are consistent with those of synthetic tests. Both deconvolution methods result in delta-function-like and well-aligned  $P$  signals; however, the array-deconvolved ones appear sharper, indicating the effectiveness of the array deconvolution in collapsing the signal into a spike. On the  $SV$  components, coherent signals at  $\sim 4.8$  s can be observed in all data sections, representing the conversion at the Moho. However, the array-deconvolved data appear more stable and consistent throughout, while the corresponding water level-deconvolved data are less so. In addition, a number of differences are worth noting. First, the array-deconvolved traces contain more high-frequency energy than do the water level-deconvolved ones. Second, there are traces that cannot be well resolved by water level deconvolution and that result in anomalously low-frequency signal (e.g. in the Costa Rica event,  $SV$  traces 1 and 8; in the Tonga event, traces 3, 6 and 8). In contrast, array deconvolution in general achieves more stability. We also calculate the variance, as defined in the synthetic tests, of the deconvolved data (shown as the number in the parentheses above each panel). In these four examples, the array-deconvolved data all have much smaller variances (at least one order of magnitude smaller) than those of the water level-deconvolved ones. This shows the advantage of array deconvolution in extracting coherent signals across array while attenuating noise. An additional advantage can be noted by examining the Tonga event (Fig. 7d). This event has a magnitude  $m_b = 6.3$ , but the noisy  $SV$  components with anomalous low-frequency patches has prevented it from being used in the previous RF analysis. Using the array deconvolution, however, we are able to attain more stable and thus usable signals from this event.

Of course, additional tweaking of the water level processing, for example, by high-pass filtering of noisy traces could reduce the

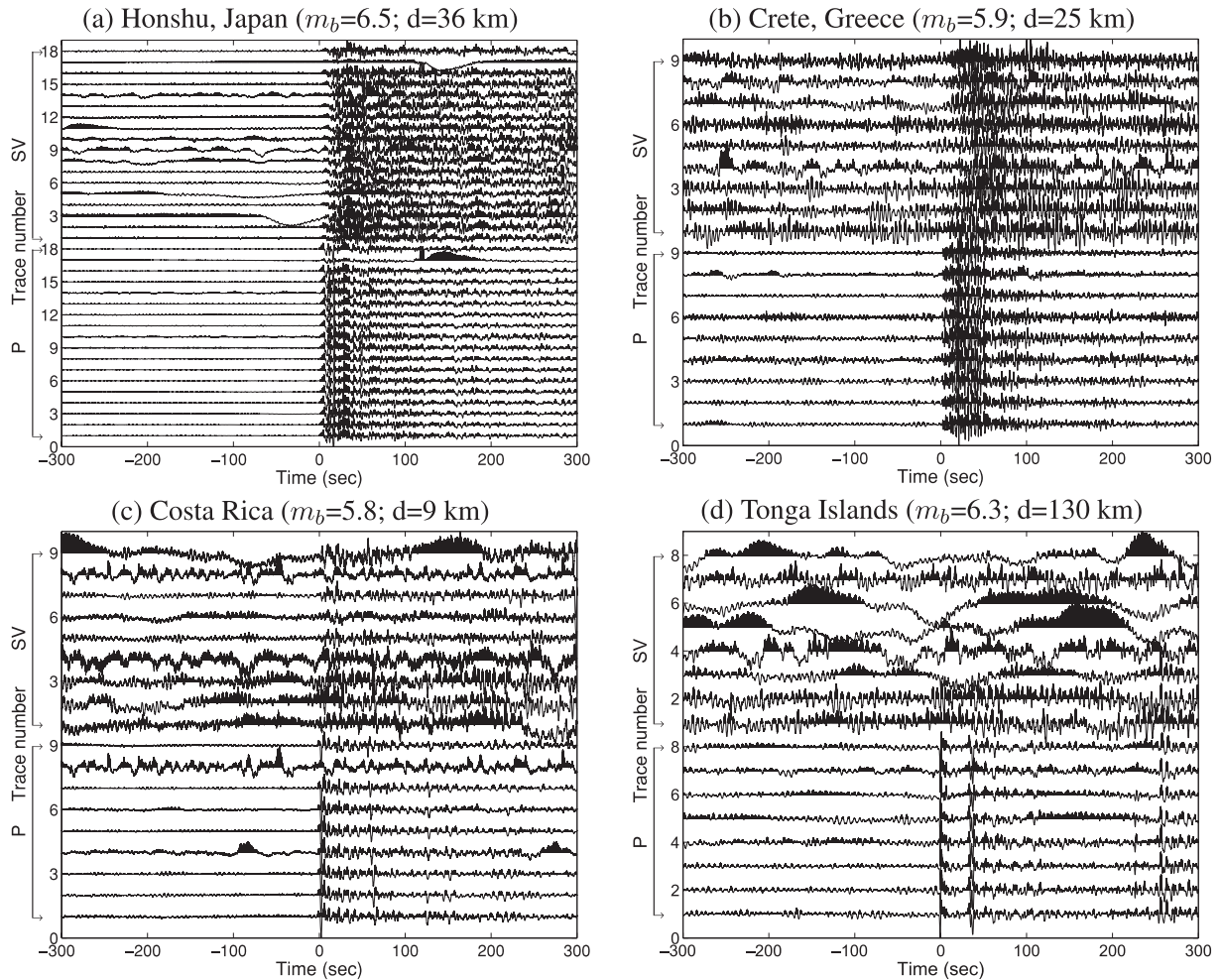


**Figure 6.** The raw data ( $P$  and  $SV$  components) of four exemplary earthquakes from (a) Honshu, Japan; (b) Crete, Greece; (c) Costa Rica and (d) Tonga Islands. Note the traces are individually normalized. The magnitude ( $m_b$ ) and depth associated with each event are also indicated.

**Table 1.** The earthquake parameters of the four exemplary events.

Date	Time	Latitude (°N)	Longitude (°E)	Depth (km)	$m_b$	$\Delta$ (°)	Baz (°)	Location
2004 January 25 (025)	11:43:11	-16.83	-174.196	129.8	6.4	94.5959	239.3742	Tonga Islands
2004 March 17 (077)	05:21:00	34.589	23.326	24.5	5.9	74.3788	38.0443	Crete, Greece
2004 June 29 (181)	07:01:30	10.738	-87.043	9	5.8	56.3828	151.9377	Costa Rica
2005 August 16 (228)	02:46:28	38.276	142.039	36	6.5	62.6444	302.5049	Honshu, Japan

*Notes:*  $\Delta$  is epicentral distance from the event to the centre of the POLARIS-MIT array. Baz is backazimuth of the event with respect to the array, counting clockwise from north.

difference between the water level and array-derived results. The main point of this paper is that such expert tweaking can be largely replaced by an automated process suitable for treating very large data sets including data with very low signal-to-noise ratios.

The processing procedure is implemented for the whole data set of 135 events. In Fig. 8, we show the deconvolved  $SV$  traces as a function of backazimuth at five receivers. We observe that, in addition to coherent signals corresponding to the Moho, there appears to be various coherent signals at different times between the surface ( $t = 0$  s) and the Moho ( $t = 4.8$  s) from receiver to receiver. These variations suggest the presence of local crustal heterogeneities beneath each receiver, and were not observed before when only limited high-quality seismic records were utilized. We also plot the decon-

volved data as a function of earthquake magnitude. An example using data from station ACKN is shown in Fig. 9. We observe that the Moho signal appears consistently visible in the entire magnitude range, and does not degrade at smaller magnitudes ( $5.5 \leq m_b < 5.8$ ). This means that the noise for these records is primarily signal-generated, consisting mainly of misaligned scattered energy (which is preserved and deconvolved in so far as it shares a signature with the direct signal) and residual energy not captured by the source estimate (due to, e.g. variable receiver response and errors in the polarization pre-processing). The data used for this study were selected before the results were known and it seems clear that the pre-selection process was excessively restrictive and that the array deconvolution can be readily applied to earthquakes with smaller

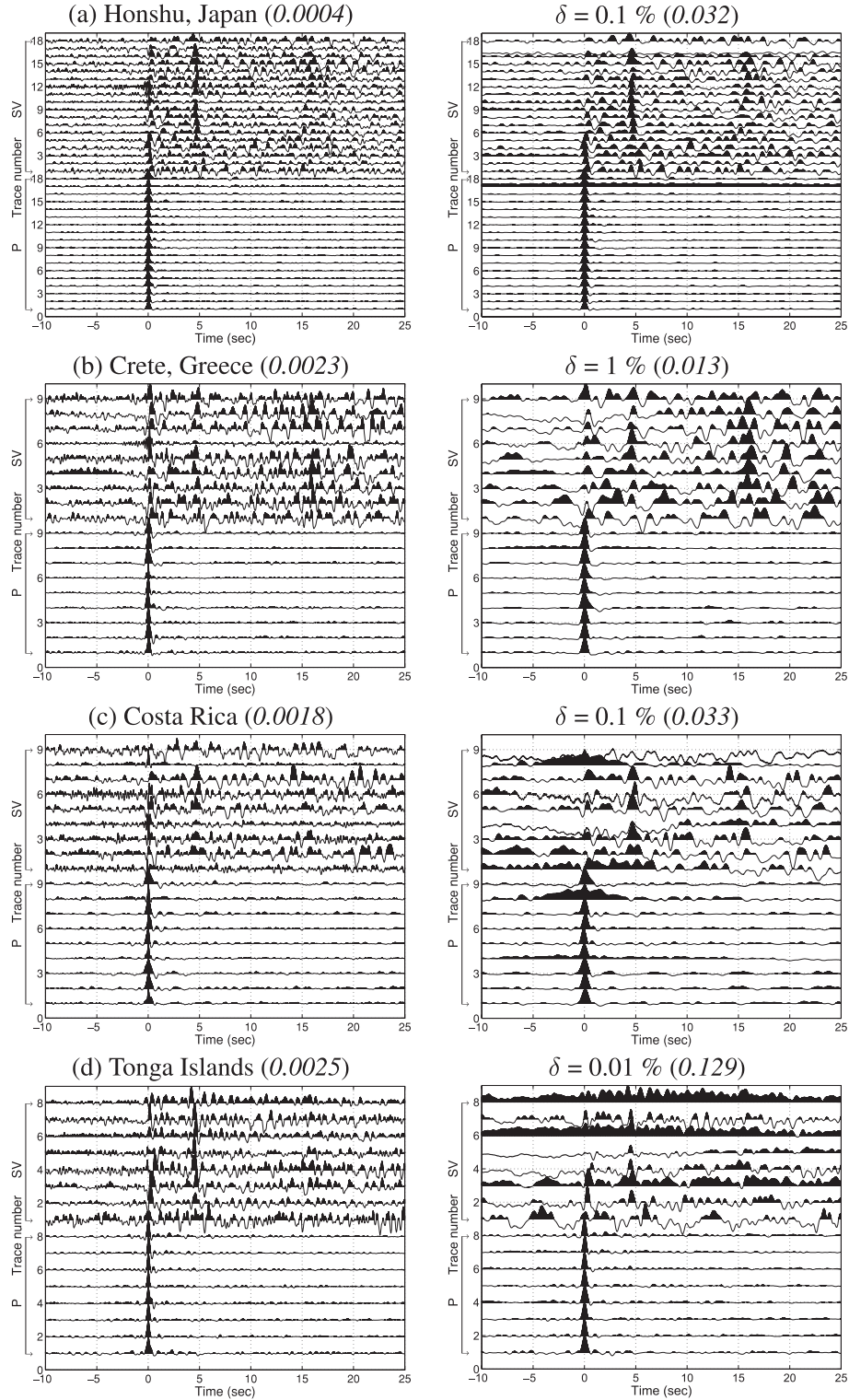


**Figure 7.** The deconvolved data of the four earthquakes shown in Fig. 6. The left-hand column shows the results from array-conditioned deconvolution. The right-hand column shows the corresponding results from water level deconvolution, denoted with the water level factor used. The choice of water level is based on the trade-off between the variance and the broadening of the signal. The number in the parentheses indicates the corresponding variance.

magnitudes. Further analysis of this application is the topic of a separate paper.

In closing, we note that, traditionally, the deconvolution has been achieved in an iterative manner, whether it is to find a ‘best’ reg-

ularization parameter in the frequency domain deconvolution, or to minimize the difference between observed and modelled data in the time domain deconvolution (e.g. Gurrola *et al.* 1995; Ligorría & Ammon 1999). In this context, the array-conditioned deconvolution

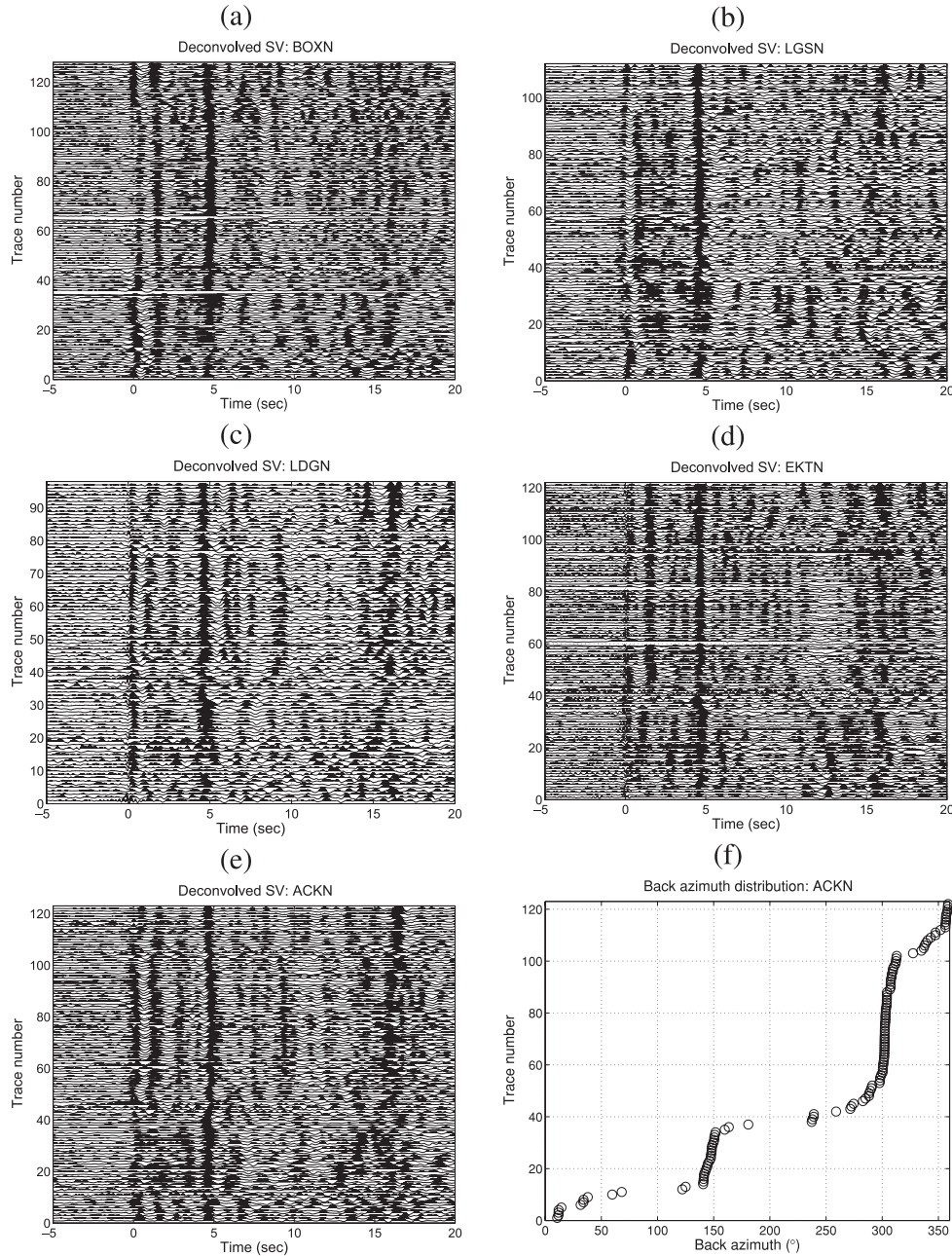


**Figure 8.** The deconvolved  $SV$  data sections of five receivers. (a) BOZN; (b) LGSN; (c) LDGN; (d) EKTN and (e) ACKN. (f) The representative backazimuthal distribution of the teleseismic events recorded at this array. A majority of earthquakes are located at the western Pacific subduction zones (around  $300^\circ$ ).

presents a new, effective and automatic means for processing large amounts of array data, as it does not require any ad-hoc regularization; the regularization is achieved naturally by using the noise present in the array itself.

## 5 CONCLUSIONS

The application of the array-conditioned deconvolution improves the efficiency and automation of the deconvolution process that is an essential step in RF analysis and in data pre-processing for imaging of scattered waves. Synthetic experiments demonstrate the effectiveness of the deconvolution technique, especially for noisy data. Application of this technique to a teleseismic data set from

the Slave craton yields a deconvolved data section that clearly identifies the  $P_S$  conversion at the Moho, and suggests the presence of local crustal heterogeneities beneath each receiver. The performance of the array deconvolution with noisy data promises the potential of exploiting earthquakes with smaller magnitudes, which would increase the number of usable sources, thus providing more comprehensive azimuthal coverage than was possible before.

## ACKNOWLEDGMENTS

We thank Gary Pavlis and an anonymous reviewer for their thoughtful comments that helped improve the clarity of this manuscript. This work was initiated and mostly carried out during a summer

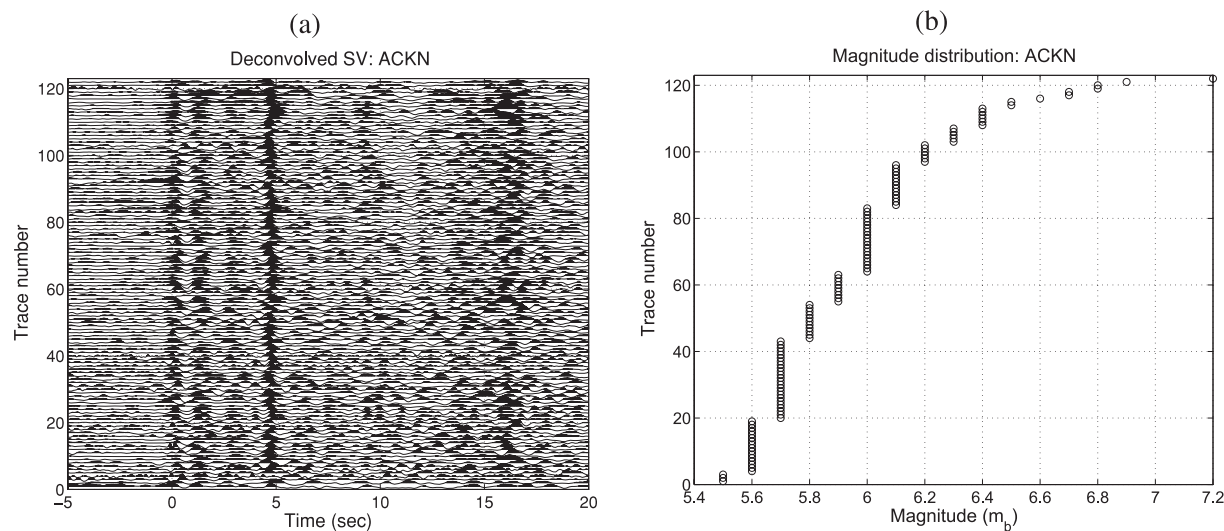


**Figure 9.** (a) The deconvolved  $SV$  data section of station ACKN plotted as a function of earthquake magnitude. (b) The distribution of traces according to magnitude.

internship of C.-W. Chen at Schlumberger-Doll Research in 2008. The POLARIS-MIT array data were collected and analysed as part of the Slave craton experiment, which was funded by the POLARIS consortium and the US National Science Foundation grant EAR-0409509 to S. Rondenay.

## REFERENCES

- Aki, K. & Richards, P.G., 2002. *Quantitative Seismology*, 2nd edn, University Science Books, Sausalito, CA.
- Berkhout, A.J., 1977. Least-squares inverse filtering and wavelet deconvolution, *Geophysics*, **42**, 1369–1383.
- Bleeker, W., Ketchum, L., Jackson, V. & Villeneuve, M., 1999. The central Slave basement complex. Part I. Its structural topology and autochthonous cover, *Can. J. Earth Sci.*, **36**, 1083–1109.
- Bostock, M.G., 1998. Mantle stratigraphy and evolution of the Slave province, *J. geophys. Res.*, **103**, 21 183–21 200.
- Bostock, M.G. & Sacchi, M.D., 1997. Deconvolution of teleseismic recordings for mantle structure, *Geophys. J. Int.*, **129**, 143–152.
- Chen, C.-W., Rondenay, S., Evans, R.L. & Snyder, D.B., 2009. Geophysical detection of relict metasomatism from an Archean (~3.5 Ga) subduction zone, *Science*, **326**, 1089–1091.
- Clayton, R.W. & Wiggins, R.A., 1976. Source shape estimation and deconvolution of teleseismic bodywaves, *Geophys. J. R. astr. Soc.*, **47**, 151–177.
- Embree, P., 1968. Diversity seismic record stacking method and system, U.S. Patent, **3**, 398,396.
- Gurrola, H., Baker, G.E. & Minster, J.B., 1995. Simultaneous time-domain deconvolution with application to the computation of receiver functions, *Geophys. J. Int.*, **120**, 537–543.
- Haldorsen, J.B.U., Miller, D.E. & Walsh, J.J., 1994. Multichannel Wiener deconvolution of vertical seismic profiles, *Geophysics*, **59**, 1500–1511.
- Haldorsen, J.B.U., Miller, D.E. & Walsh, J.J., 1995. Walk-away VSP using drill noise as a source, *Geophysics*, **60**, 978–997.
- Kennett, B.L.N., 1991. The removal of free surface interactions from three-component seismograms, *Geophys. J. Int.*, **104**, 153–163.
- Kennett, B.L.N. & Engdahl, E.R., 1991. Traveltimes for global earthquake location and phase identification, *Geophys. J. Int.*, **105**, 429–465.
- Langston, C., 1979. Structure under Mount Rainier, Washington, inferred from teleseismic body waves, *J. geophys. Res.*, **84**, 4749–4762.
- Li, X.-Q. & Nábělek, J.L., 1999. Deconvolution of teleseismic body waves for enhancing structure beneath a seismometer array, *Bull. seism. Soc. Am.*, **89**, 190–201.
- Ligorria, J.P., Ammon, C.J., 1999. Iterative deconvolution and receiver-function estimation, *Bull. seism. Soc. Am.*, **89**, 1395–1400.
- Neal, S.L. & Pavlis, G.L., 1999. Imaging  $P$ -to- $S$  conversions with multichannel receiver functions, *Geophys. Res. Lett.*, **26**, 2581–2584.
- Neal, S.L. & Pavlis, G.L., 2001. Imaging  $P$ -to- $S$  conversions with broadband seismic arrays using multichannel time-domain deconvolution, *Geophys. J. Int.*, **147**, 57–67.
- Press, W.H., Teukolsky, S.A., Vetterling, W.T. & Flannery, B.P., 1992. *Numerical Recipes*, 2nd edn, 992 pp, Cambridge University Press, Cambridge.
- Rondenay, S., 2009. Upper mantle imaging with array recordings of converted and scattered teleseismic waves, *Surv. Geophys.*, **30**, 377–405, doi:10.1007/s10712-009-9071-5.
- Rondenay, S., Bostock, M.G. & Fischer, K.M., 2005. Multichannel inversion of scattered teleseismic body waves: practical considerations in *Seismic Earth: Array analysis of broadband seismograms*, Vol. 157, pp. 187–204, eds Levander A. & Nolet G., AGU Geophysical Monograph Series.
- Ulrych, T.J., Sacchi, M.D. & Freire, S.L.M., 1999. Eigenimage processing of seismic sections, in *Covariance Analysis for Seismic Signal Processing*, *Geophys. Development*, 8, Soc. Exploration Geophysicists, 978–997.
- Vinnik, L.P., 1977. Detection of waves converted from  $P$  to  $SV$  in the mantle, *Phys. Earth planet. Inter.*, **15**, 39–45.